AIChE

In Situ Crystallization to Zinc Aluminate Films with Controlled Surface Microstructure and Anticorrosion Performance

Guoli Fan and Feng Li
State Key Laboratory of Chemical Resource Engineering, Beijing University of Chemical Technology,
Beijing 100029, People's Republic of China

DOI 10.1002/aic.12781

Spinel-type zinc aluminate ($ZnAl_2O_4$) thin films with controlled surface microstructure on aluminum substrates were fabricated via a facile and effective in situ crystallization method without using any templates or surfactants. The surface microstructure of $ZnAl_2O_4$ films could be significantly controlled by varying the experimental conditions including concentration of reactants, crystallization temperature, and crystallization time. After surface modification, the specific topography of $ZnAl_2O_4$ films was beneficial to obtain surface hydrophobic or superhydrophobic properties. More importantly, compared to nanoparticle- and nanosword-assembled $ZnAl_2O_4$ films, nanorod-assembled $ZnAl_2O_4$ film provided a more effective barrier to aggressive species for aluminum substrates in a wide range of pH values; very low corrosion current density of the order of $\sim 10^{-9}$ A cm^{-2} could be achieved. A new contribution to the development of advanced coating system with $ZnAl_2O_4$ film materials that can be used in practical application for corrosion protection of aluminum materials is provided. © 2011 American Institute of Chemical Engineers *AIChE J,* 58: 2639–2649, 2012

Keywords: zinc aluminate, thin films, microstructure, hydrophobicity, corrosion resistance

Introduction

Spinel-type AB_2O_4 complex metal oxides, as an important class of functional inorganic materials, have attracted extensive attention in past two decades, due to their excellent applications in optoelectronics,[1–5] gas sensors,[6,7] medicines,[8,9] magnetic devices,[10,11] catalyst supports,[12–14] and catalysts.[15–17] Recently, tremendous efforts have been directed toward the controlled growth of spinel nanostructures, which provides the flexibility for tailoring their physicochemical properties according to special applications.[18–20] As for spinel-type oxide films, their unique surface topography can significantly affect the mechanical, optical, electrical, and biological properties of materials.[21,22]

Zinc aluminate ($ZnAl_2O_4$), well-known as a wide band gap semiconductor (3.8 eV), has been widely used as dielectric materials due to its desirable properties, such as high mechanical and chemical resistance, high thermal stability, etc.[23–25] Historically, there were a number of research works for preparing $ZnAl_2O_4$ fine powders by conventional solid-state route,[26–28] chemical vapor deposition,[29] sol-gel technique,[30,31] and hydrothermal method.[32–34] However, there are few reports on the fabrication of continuous $ZnAl_2O_4$ films, mainly owing to the difficulty in controlling the precipitation rate of films.[35–38] For instance, Wu et al.[36] prepared interconnected microstructural $ZnAl_2O_4$ films on silicon substrates via a sol-gel route using aluminum tri-*sec*-butoxide as the source of Al and hexylene glycol as a solvent. Recently, Tian et al.[38] also synthesized mesoporous $ZnAl_2O_4$ films through evaporation-induced method using triblock copolymer pluronic F-127 as structure-directing agent. Moreover, rare-earth-doped $ZnAl_2O_4$ films could be prepared by spray pyrolysis technique.[37] Generally, these methods need complicated processing and/or specialized equipments. In most cases, they require handling of large amount of organic salts, toxic solvents, or surfactants, which cause expensive costs as well as environment pollution. Therefore, the above physical and chemical methods are not suitable for environmentally benign scale-up synthesis. Owing to the uncontrollable phase separation during multicomponent reactions and poor adhesion to underlying substrate, a challenge still remains to develop more effective protocols for the microstructure control of $ZnAl_2O_4$ films and further the performance of new applications in various fields such as advanced catalysts, gas sensors, and coating materials.

Conversely, it is known that the aluminum and aluminum alloys are highly susceptible to localized corrosion, especially in chloride-containing environments. Over the years, the development of diverse active corrosion protection systems or strategies for preventing the degradation processes of metallic substrates has been an issue of prime importance for industrial applications.[39,40] Among them, anodization is thought to be an affective way of corrosion protection by thick oxide layer formed on substrate.[41] However, because of the porous nature, the oxide layer cannot provide adequate barrier property to prevent the ingress of corrosive species onto the metal surface.[42] Another approach of corrosion protection is achieved by deposition of organic barrier

---

Correspondence concerning this article should be addressed to F. Li at lifeng_70@163.com.

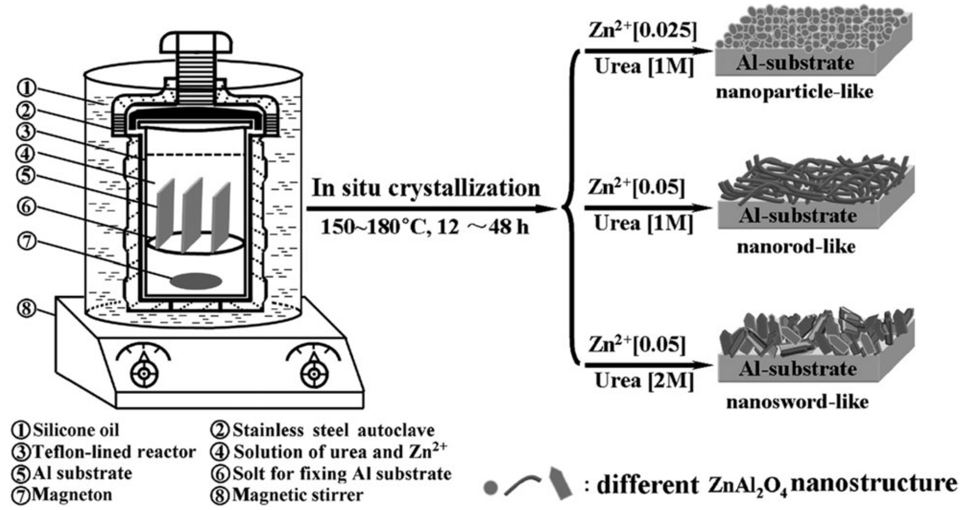

Figure 1. Schematic illustration of the formation process of $ZnAl_2O_4$ nanostructures on the aluminum substrates.

coatings on substrate, which can prevent contact of the metal with the corrosive environment.[43,44] Usually, adhesion of organic coatings is far away from satisfactory unless special pretreatment like chromate coating is used.[45,46] However, the carcinogenic nature of chromate coating limits its use. Therefore, the development of a new approach to introduce environmentally friendly corrosion protection coating systems with excellent performance becomes an urgent need for many industries.

In this article, we reported the first example of direct fabrication of $ZnAl_2O_4$ films using aluminum foil as both the substrate and sole aluminum source. The surface microstructure of the obtained $ZnAl_2O_4$ films can be controlled via a facile and effective *in situ* crystallization approach without using any templates or surfactants. The formation process of the nanostructure-assembled $ZnAl_2O_4$ films on aluminum substrates is schematically illustrated in Figure 1. The effects of concentration of reactants, crystallization time, and crystallization temperature on the surface morphologies of $ZnAl_2O_4$ films were investigated. More significantly, it is found that the resulting $ZnAl_2O_4$ films could adhere strongly to the substrate and provide effective corrosion-resistant coating for the underlying aluminum. To the best of our knowledge, there are no reports on *in situ* fabrication of $ZnAl_2O_4$ thin films with controlled nanostructures and resulting anticorrosion protection for aluminum substrates.

Experimental

Materials

Aluminum foils (purity: >99.99% and thickness: 0.26 mm) purchased from Beijing Jing Xi Chemical Technology were cut into square pieces with a size of 20 mm × 20 mm as Al substrates. First, Al substrates were treated in dilute HCl solution (1.0 M) for 2 min at room-temperature and rinsed with distilled water to remove the surface oxide layer. Subsequently, substrates were ultrasonically cleaned in acetone to remove the surface organic contaminations, and finally air-dried.

Fabrication of spinel-type $ZnAl_2O_4$ thin films

$ZnAl_2O_4$ thin films with different surface microstructures were fabricated by one-step *in situ* crystallization on Al substrates. In a typical procedure, $Zn(NO_3)_2 \cdot 6H_2O$ (2.0 mmol) and urea (80 mmol) were dissolved in 80 mL of water/ethanol mixture solvent (v/v = 1/1) to form a clear solution ($[Zn^{2+}] = 0.025$ M and [urea] = 1.0 M). The resulting solution was transferred into 100 mL of Teflon-lined autoclave with an inner diameter of 4.0 cm, where the treated Al substrates were vertically fixed onto a slot (Figure 1). Subsequently, the autoclave was placed into an oil bath and stirred magnetically with a rate of about 200 rpm, and then heated at 180°C for 24 h. After cooling, the resulting $ZnAl_2O_4$ films were rinsed with ethanol and dried at ambient temperature. The microstructure control experiments of $ZnAl_2O_4$ films were carried out in a similar process by changing the synthesis parameters including concentration of reactants, crystallization temperature, and crystallization time (Table 1). The surface hydrophobization of as-fabricated $ZnAl_2O_4$ films was performed by immersion in 0.05 M sodium laurate aqueous solution at 70°C for 12 h. After immersion, the films were rinsed with ethanol and dried at ambient temperature.

Characterization

Powder X-ray diffraction (XRD) patterns of film samples with a size of about 5 mm × 5 mm were directly collected using a Shimadzu XRD-6000 diffractometer under the following conditions: 40 kV, 30 mA, graphite-filtered Cu $K\alpha$ radiation. The samples were step-scanned in steps of 0.04° (2θ) using a count time of 10 s/step.

Field emission scanning electron microscopy (FESEM) of samples was directly carried out on a Zeiss Supra 55 instrument with an accelerating voltage of 20 kV. Before FESEM observation, films were sputtered with gold to provide a conducting surface.

Transmission electron microscopy (TEM) was taken using a JEOL-2100 transmission electron microscope operated at 100 kV. For TEM analysis, $ZnAl_2O_4$ powders scraped from the surface of films were dispersed in ethanol. A droplet of the ultrasonically dispersed powders was placed onto an amorphous carbon-coated copper grid and dried at ambient temperature. High-resolution transmission electron microscopy (HRTEM) was carried out at an accelerating voltage of 200 kV.

Room-temperature Fourier transform infrared (FTIR) spectrum was recorded in the range of 4000–400 cm^{-1} with 2 cm^{-1} resolution on a Bruker Vector-22 Fourier transform

Table 1. The Synthesis Parameters and Morphologies of As-Fabricated $ZnAl_2O_4$ Films on Aluminum Substrates

Samples	Zn^{2+} (M)	Urea (M)	Crystallization Time (h)	Crystallization Temperature (°C)	Morphology
ZA-a	0.025	1	24	180	Nanoparticle
ZA-b	0.05	1	24	180	Nanorod
ZA-c	0.05	2	24	180	Nanosword
ZA-d	0.05	2	24	60	Curved nanosheet
ZA-e	0.05	2	24	150	Irregular nanosheet
ZA-f	0.025	1	12	180	Nanoparticle
ZA-g	0.05	1	12	180	Nanorod
ZA-h	0.05	2	12	180	Nanosword
ZA-i	0.025	1	48	180	Nanoparticle
ZA-j	0.05	1	48	180	Nanorod
ZA-k	0.05	2	48	180	Nanosword

spectrometer using the KBr pellet technique (1 mg of sample in 100 mg of KBr).

Atomic force microscopy (AFM) micrograph was taken on a DI nanoscope IV (Digital Instruments) using the tapping mode at a resolution of 2 nm in *X–Y* and 0.1 nm in *Z* orientation.

Static water contact angle (CA) of samples was measured on a commercial drop-shape analyses system (DSA 100, KüRSS GmbH, Germany) at ambient temperature. The equilibrium water CA was measured with a fixed needle supplying a water drop of 5 μL, and five different points on each sample were investigated.

X-ray photoelectron spectroscopy (XPS) was performed on a VG ESCALAB MKII spectrometer with a monochromatic Al Kα X-ray radiation (1486.6 eV photons). The depth profiling experiment was conducted at argon partial pressure of 10^{-6} Torr, while applying 4 kV voltage at an ion beam current of 10 mA cm^2, resulting in a ~0.5-nm/min etching rate. Binding energies were calibrated based on graphite C 1s peak at 284.6 eV.

Corrosion-resistant property evaluations

A conventional three-electrode configuration was used with the $ZnAl_2O_4$ films under test as the working electrode with an area of 1.0 cm^2, a platinum electrode as the counter electrode, and a saturated calomel electrode as the reference electrode. Aqueous sodium chloride solution (3.5%) was used as the electrolyte. The samples were immersed in the corrosive medium for 30 min before the electrochemical tests to ensure the steady state. The pH value was adjusted by adding diluted hydrochloric acid (1.0 M) and sodium hydroxide (1.0 M). The Tafel polarization tests were recorded with a CHI 660C electrochemical workstation at room-temperature at a sweep rate of 10 mV s^{-1}. The electrochemical impedance spectroscopy (EIS) data were acquired at open circuit potential applying a 10 mV sinusoidal perturbation in the 100 kHz–10 mHz frequency range at room-temperature.

Results and Discussion

Fabrication and characterization of $ZnAl_2O_4$ thin films

The different types of $ZnAl_2O_4$ nanostructures were grown on Al substrates by varying concentrations of reactants, crystallization time, and crystallization temperature (Table 1). Figure 2a shows the XRD patterns of three representative $ZnAl_2O_4$ film samples (ZA-a, ZA-b, and ZA-c). The samples indicate the identical characteristic (220), (311), (422), and (511) reflections of cubic spinel-type $ZnAl_2O_4$ phase (JCPDS no. 05-0669), except for the reflections from Al substrates. Figure 2b depicts the FTIR spectrum of $ZnAl_2O_4$ powder scraped from ZA-b sample. In detail, a strong and broad absorption band centered at around 3421 cm^{-1} can be identified as the hydroxyl stretching band $\nu(OH_{str})$, arising from absorption water molecules. Another absorption band resulting from the hydroxyl deformation mode of water, $\delta(H_2O)$, is recorded at around 1625 cm^{-1}. There are two strong characteristic absorption peaks at about 558 and 677 cm^{-1}, which can be assigned to the stretching vibrations of the metal–oxygen bonds for spinel structure in tetrahedral positions and octahedral positions, respectively.[30,47] The aforementioned confirms that the obtained products on Al substrates are pure-phase $ZnAl_2O_4$.

The surface morphologies of $ZnAl_2O_4$ films were investigated by FESEM micrographs. From FESEM micrograph of ZA-a sample (Figure 3a), it can be seen that a large number of nanoparticles are closely stacked together and homogeneously distributed on the substrate surface. According to FESEM micrographs, the average particle size of ZA-a

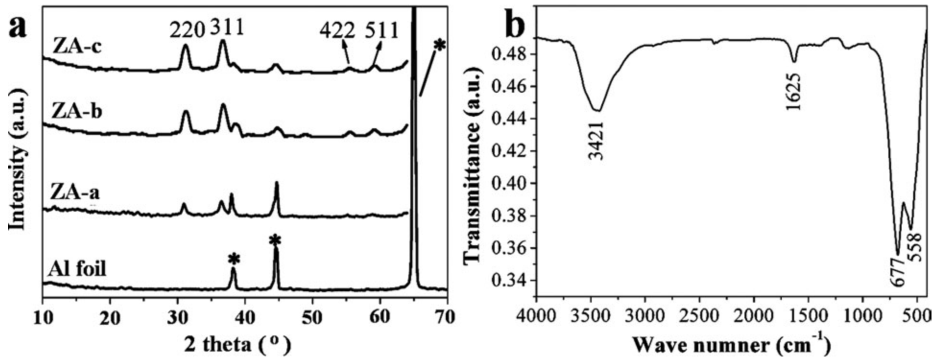

Figure 2. XRD patterns of as-fabricated $ZnAl_2O_4$ films (a), and * indicates the reflection peaks from the aluminum substrate; FTIR spectrum of ZA-b film sample (b).

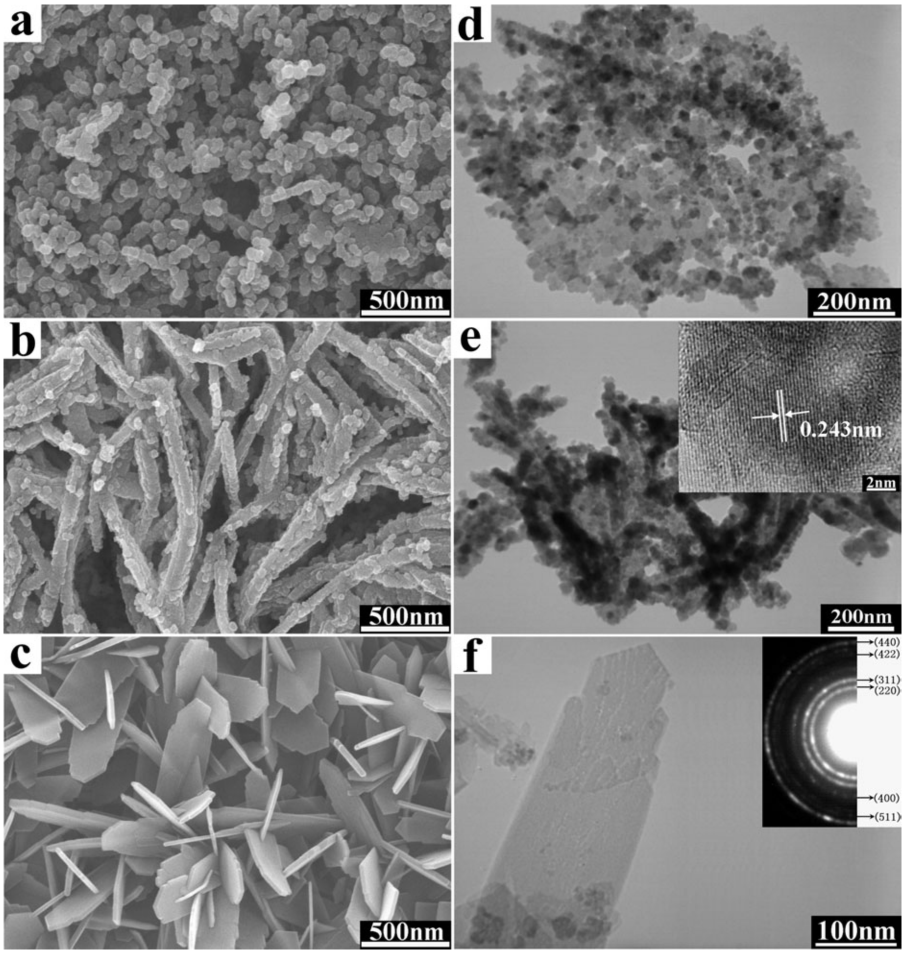

Figure 3. FESEM micrographs of $ZnAl_2O_4$ film samples.

ZA-a (a), ZA-b (b), and ZA-c (c); TEM micrograph of nanoparticles scraped from ZA-a (d); TEM micrograph of nanorods scraped from ZA-b (e), and inset shows HRTEM micrograph of an individual nanorods; TEM micrograph of nanoswords scraped from ZA-c (f), and inset shows the corresponding SAED image of an individual nanosword.

sample estimated from no less than 100 particles is about 38 ± 5 nm. ZA-b sample presents the morphology of nanorods with a diameter of about 50–80 nm and a length of about 1.5–3.0 μm (Figure 3b), while ZA-c sample shows the morphology of nanoswords with a lateral size of about 150–250 nm and a thickness of about 20–30 nm (Figure 3c).

The $ZnAl_2O_4$ nanostructures grown on Al substrates were investigated by TEM and HRTEM micrographs. As shown in Figure 3d, $ZnAl_2O_4$ layer in ZA-a presents the character of nanoparticles with a diameter of about 20 nm. However, as for ZA-b sample, numerous nanoparticles (10–20 nm) interconnect with each other along the rod axis to self-assemble into larger rod-like morphology (Figure 3e). Further, close inspection of representative HRTEM micrograph of an individual nanorod clearly reveals the presence of an interplanar distance of about 0.243 nm that is characteristic of (311) plane of $ZnAl_2O_4$ phase (inset in Figure 3e). Interestingly, $ZnAl_2O_4$ layer in ZA-c shows nanosword-like shape (Figure 3f). Additionally, selected area electron diffraction (SAED) pattern of an individual nanosword (inset in Figure 3f) substantiates six discernible diffraction characteristic rings corresponding to cubic $ZnAl_2O_4$ phase, confirming the polycrystalline nature of $ZnAl_2O_4$ layers.

The surface microstructure of as-fabricated $ZnAl_2O_4$ films was characterized by AFM images (Figure 4). Two-dimensional AFM images (Figures 4a–c) reveal that distinct protrusions and pitches present on the rough surface of films. The root-mean-square roughness of the films is estimated to be 51, 144, and 263 nm for ZA-a, ZA-b, and ZA-c, respectively, well in agreement with the change in the surface pattern from nanoparticles to nanorods and nanoswords. Moreover, small bulges in ZA-a, ravines in ZA-b, and isolated triangular islands in ZA-c can be resolved in the three-dimensional AFM images (Figures 4d–f). The bulges and ravines result from the close adherence and assembly of numerous nanoparticles and nanorods, respectively, while the isolated triangular islands are attributed to the vertex of some perpendicular nanoswords. In light of the particular surface topography of the as-fabricated $ZnAl_2O_4$ films, it can, therefore, be expected to design hydrophobic surfaces. It can be observed that when a water droplet is dropped onto $ZnAl_2O_4$ film on substrate, it spreads very quickly over the surface with low water CA of about 8° (Figure 5a), indicating the surface hydrophilicity of this film due to ‘‘high-energy interface’’ for metal oxide. Nevertheless, when the surface of $ZnAl_2O_4$ films is modified by simple immersion in an aqueous solution of sodium laurate, the water CA increases gradually from 139 ± 2° for ZA-a to 145 ± 2° for ZA-b, and 153 ± 2° for ZA-c (Figures 5b–d), indicative of high surface hydrophobicity for ZA-a and ZA-b, and even

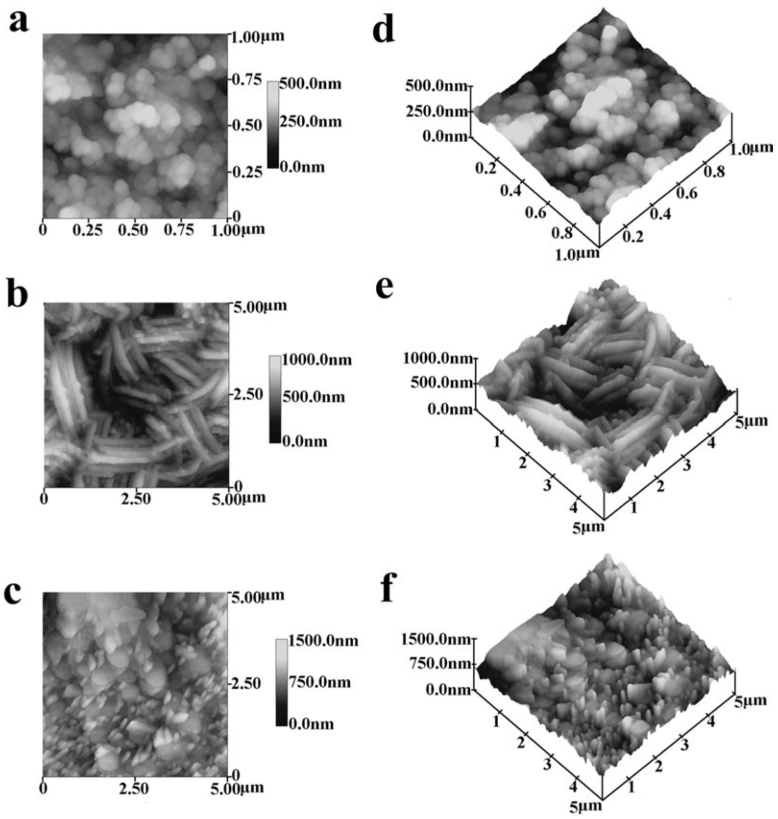

Figure 4. Two-dimensional AFM images of $ZnAl_2O_4$ films.

ZA-a (a), ZA-b (b), and ZA-c (c); three-dimensional AFM images of $ZnAl_2O_4$ films: ZA-a (d), ZA-b (e), and ZA-c (f).

surface superhydrophobicity for ZA-c with the water CA higher than 150°. The enhanced hydrophobic properties can be mainly ascribed to the increasing surface roughness of $ZnAl_2O_4$ films.[48–50]

XPS measurements within a binding energies range of 0–1200 eV were performed to investigate the surface/near-surface chemical states and the thickness of the $ZnAl_2O_4$ layers on Al substrates. The representative XPS result of ZA-b sample is shown in Figure 6. It is observed from the inset of Figure 6a that there are two photoemission peaks centered at about 1021.5 and 1044.7 eV, which are attributed to Zn $2p_{3/2}$ and Zn $2p_{1/2}$ of surface $ZnAl_2O_4$ layers, respectively. The depth profile analysis by Ar^+ sputtering collected across the film reveals an obvious distribution gradient of the Zn concentration, which gives a film thickness of about 270 nm for ZA-b. In particular, the Zn/(Zn + Al + O) molar ratios of about 14% at the outermost surface of $ZnAl_2O_4$ film match well with the nominal molar ratio of spinel phase. In the three-dimensional Al 2p XPS spectra, based on different Ar^+ sputtering time (Figure 6b), a small peak at 75.6 eV resulting from the tetrahedral coordination of amorphous Al_2O_3 can be detected at the uppermost surface of Al substrate,[51] while the main peak centered at 74.0 eV is associated with the octahedral coordination of aluminum species.[35] The presence of continuous ultrathin $ZnAl_2O_4$ layers of smaller than 300 nm in thickness implies that the *in situ* growth of $ZnAl_2O_4$ only occurs in the surface regions of the substrate and is diffusion-limited.

Formation mechanism of $ZnAl_2O_4$ thin films

In the present system, to avoid the effect of the gradients of temperature and concentration of reaction system on the growth of $ZnAl_2O_4$ thin films, the magnetic stirring with a rate of about 200 rpm was applied. In addition, it is well-known that the operating pressure in solvothermal reaction is related to the compactness of the autoclave and reaction temperature. Because of the fixed compactness of 80% in our case, only the operating pressure changed with the reaction temperature. Assuming that the vaporization enthalpies of water and ethanol vary slightly with temperature and the solvents in the autoclave are considered as ideal liquids, the operating pressures for the present synthesis system estimated by the Clausius–Clapeyron equation and Raoult's law are about 0.9 MPa for 150°C and 1.5 MPa for 180°C, respectively.[52,53]

To clearly understand the growth process of $ZnAl_2O_4$ film, the crystallization temperature was varied (Table 1). Typically, to take the preparation of $ZnAl_2O_4$ films using 0.05 M Zn^{2+} and 2 M urea as an example, numerous irregular curved nanosheets with the thickness of about 10–20 nm are randomly grown on the surface of the substrate at the low crystallization temperature of 60°C (Figure 7a). When the crystallization temperature reaches 150°C, the resulting film is composed of a large number of nanosheets with irregular edges and coarse surfaces and some nanoparticles (Figure 7b), as a result of fast growth of $ZnAl_2O_4$ crystals at high-temperature on the basis of the kinetics and

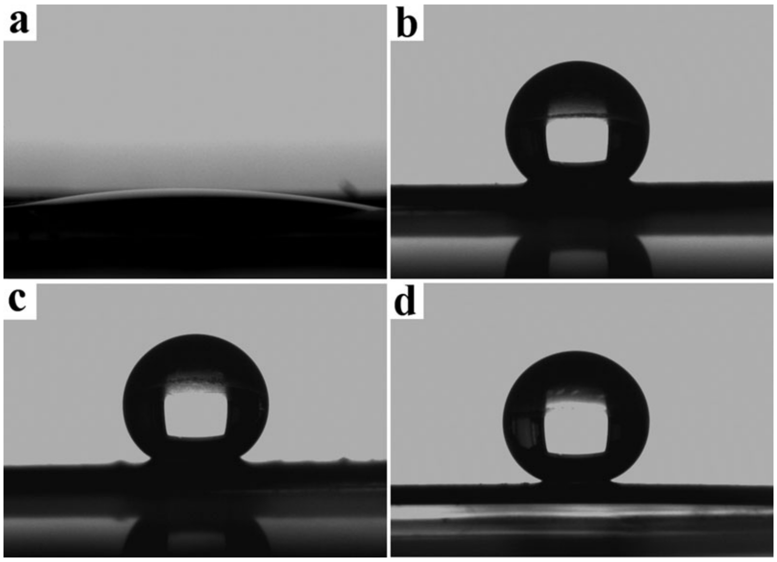

Figure 5. Shapes of water droplets over the surface of the as-fabricated $ZnAl_2O_4$ films (a), hydrophobic ZA-a (b), hydrophobic ZA-b (c), and hydrophobic ZA-c (d), revealing a CA of about 8°, 139°, 145°, and 153°, respectively.

thermodynamics of crystal growth. Further increasing the temperature to 180°C, sword-like nanosheets with almost parallel edges and smooth surface are formed on the substrate surface (Figure 7c). In addition, the increase in the stacking thickness of nanosheets with the crystallization temperature can be observed.

Besides, the effect of the crystallization time on the growth of $ZnAl_2O_4$ nanostructures on substrates was investigated (Table 1). It is found that with increasing the crystallization time from 12 to 48 h, there is no significant difference in the morphologies of $ZnAl_2O_4$ films in each case, but the crystal size and regularity of particle-like, rod-like, and sword-like $ZnAl_2O_4$ nanostructures can be improved gradually (Figures 7d–i), which is attributed to the growth–dissolution–reorganization process (Ostwald ripening) of $ZnAl_2O_4$ crystallites.[54]

In tandem with the above experimental observations, one possible growth mechanism for the $ZnAl_2O_4$ films is proposed. The chemical reactions involved were believed to proceed as follows (Eqs. 1–4)

$$CO(NH_2)_2 + 3H_2O \rightarrow 2NH_4{}^+ + CO_2 + 2OH^- \quad (1)$$

$$4Al + 3O_2 + 6H_2O + 4OH^- \rightarrow 4[Al(OH)_4]^- \quad (2)$$

$$Zn^{2+} + 2OH^- \rightarrow Zn(OH)_2 \quad (3)$$

$$Zn(OH)_2 + 2[Al(OH)_4]^- \rightarrow ZnAl_2O_4 + 2OH^- + 4H_2O \quad (4)$$

At the beginning of the growth, urea hydrolyzes to give $NH_4{}^+$, CO_2, and OH^- with the increase of pH value at the elevated reaction temperatures (Eq. 1). It is well-known that aluminum in air or under humid conditions can be oxidized by oxygen and the reaction is very slow due to the formation of an oxide passivation layer on the surface. However, the oxidation may be accelerated intensely in the presence of alkali solution, and, thus, Al^{3+} can quickly enter the solution in the form of $[Al(OH)_4]^-$ complex. In our case, because of the high OH^- concentration in the solution and the presence of dissolved oxygen, Al^{3+} ions can be released continuously into the reaction system in the form of $Al(OH)_4{}^-$ complex by chemical etching of aluminum substrate under solvothermal conditions

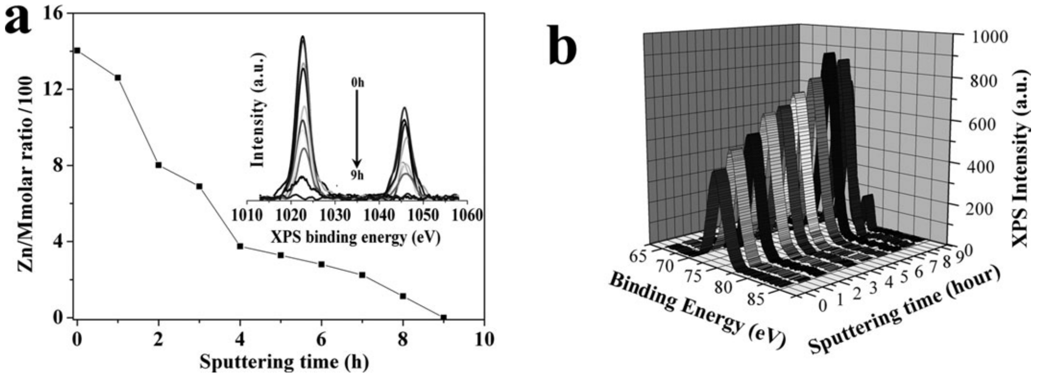

Figure 6. The molar ratio of Zn/M (M = Zn + Al + O) of ZA-b (a) as a function of film depth expressed in terms of sputtering time, and inset is the corresponding depth profile of the Zn 2p spectra with *in situ* Ar^+ sputtering at different times.

Three-dimensional depth profile of Al 2p XPS spectra of ZA-b (b) at different Ar^+ sputtering time.

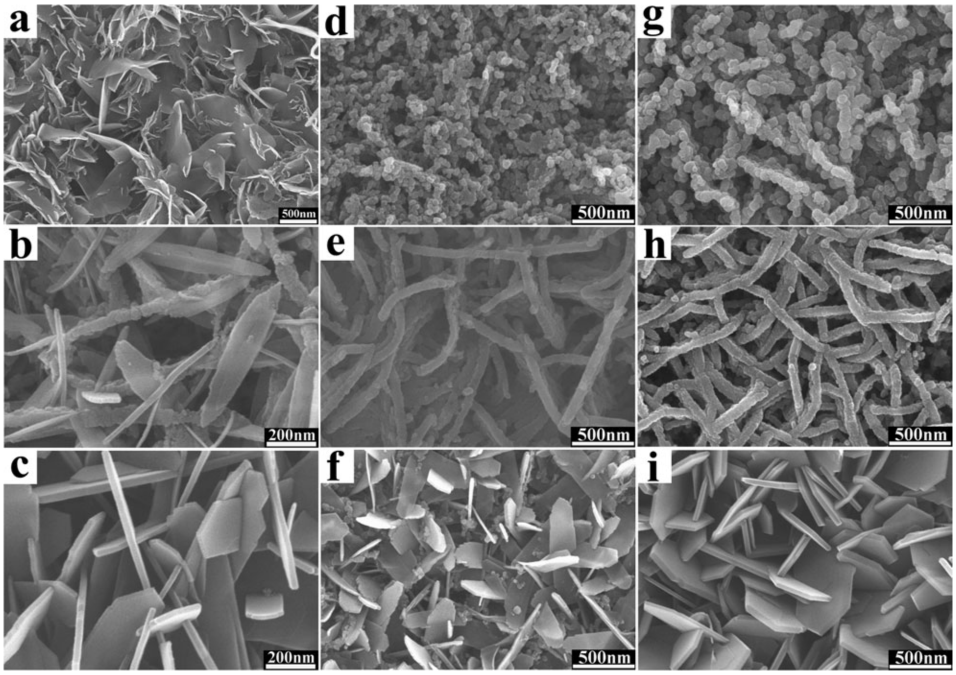

Figure 7. FESEM micrographs of $ZnAl_2O_4$ films fabricated under different experimental conditions.

ZA-d (a), ZA-e (b), ZA-c (c), ZA-f (d), ZA-g (e), ZA-h (f), ZA-i (g), ZA-j (h), and ZA-k (i).

(Eq. 2), while Zn^{2+} cations immediately react with OH^- to form $Zn(OH)_2$ (Eq. 3). Subsequently, $ZnAl_2O_4$ nuclei are formed through the structural transformation of $Zn(OH)_2$ and $Al(OH)_4^-$ intermediates generated in the solution (Eq. 4) and deposited on the substrate surface as the growth centers for crystallization.[55,56] The mixture solvent of ethanol and water can prevent the aluminum substrate from collapsing and, thus, activates the surfaces of the substrate to certain extent, which is further supported by the fact that no $ZnAl_2O_4$ film is formed with the addition of sodium hydroxide instead of urea under hydrothermal conditions in the absence of ethanol. Finally, the fusion of adjacent $ZnAl_2O_4$ crystals along the crystal plane with the lowest lattice-free energy and the growth of $ZnAl_2O_4$ crystals construct $ZnAl_2O_4$ films with different surface patterns.[57,58] According to the above Eqs. 1–4, the higher crystallization temperature can accelerate hydrolysis of urea under the solvothermal conditions, thus, leading to the increase in the concentration of OH^- ions in the solution and the etching rate of aluminum from the substrate. Meanwhile, the higher initial urea and Zn^{2+} concentrations would be advantageous for the formation of $ZnAl_2O_4$ films with high integrality of surface patterns.[59] Therefore, the prevailing growth morphology of the $ZnAl_2O_4$ architectures is strongly influenced by the degree of supersaturation under solvothermal condition, which is mainly determined by the urea and Zn^{2+} concentrations and the crystallization temperature. Certainly, during the long growth time, crystallization goes on at the substrate surfaces so long as an initial morphology of $ZnAl_2O_4$ nanostructure is maintained.

As a result, *in situ* crystallization yields high-quality $ZnAl_2O_4$ nanostructures with high purity on the substrates. Although the exact formation mechanism for the different $ZnAl_2O_4$ architectures on substrate still remains elusive, the higher free energy of initial crystalline $ZnAl_2O_4$ nanoparticles is believed to drive the crystal growth of resulting nanorod-like and nanosword-like $ZnAl_2O_4$ architectures. The self-assembly fabrication of $ZnAl_2O_4$ nanostructures from small nanoparticles is driven by a reduction of surface energy. The directed growth is limited by the stability of the nanostructures, and, thus, the size and shape of the resulting $ZnAl_2O_4$ nanorods and nanoswords are relatively uniform. In addition, compared to other $ZnAl_2O_4$ films reported in the literature,[35–38] as-fabricated $ZnAl_2O_4$ films prepared by the present method show more multifarious and excellent surface nanostructures, which can lead to the enhanced efficiency in the physicochemical performance.

Anticorrosion performance of $ZnAl_2O_4$ thin films

The anticorrosion performance of as-fabricated $ZnAl_2O_4$ films for the underlying aluminum is investigated by linear polarization measurements in a corrosive environment of neutral 3.5% aqueous sodium chloride solution at room-temperature, where chloride ions are known as an aggressive pitting corrosion species. In a typical Tafel polarization curve, the values of voltage and current density at the intersection of Tafel slopes are known as the corrosion potential and the corrosion current. The corrosion current density (corrosion current per area unit) is directly proportional to the corrosion rate. Therefore, the lower corrosion current density corresponds to the lower corrosion rate and, thus, better corrosion resistance. As shown in Figure 8a, in the passive region of polarization curves, ZA-a and ZA-b samples exhibit about three orders of magnitude reduction in polarization current as low as about 10^{-9} A cm^{-2}, compared to the bare Al substrate, indicative of significant corrosion resistance of aluminum. Such low current densities have been infrequently observed previously for pristine metal oxide coating materials or their powder counterparts.[60] A slightly increased polarization current, however, occurs for ZA-c sample. Moreover, the open circuit potential of ZA-b sample is found

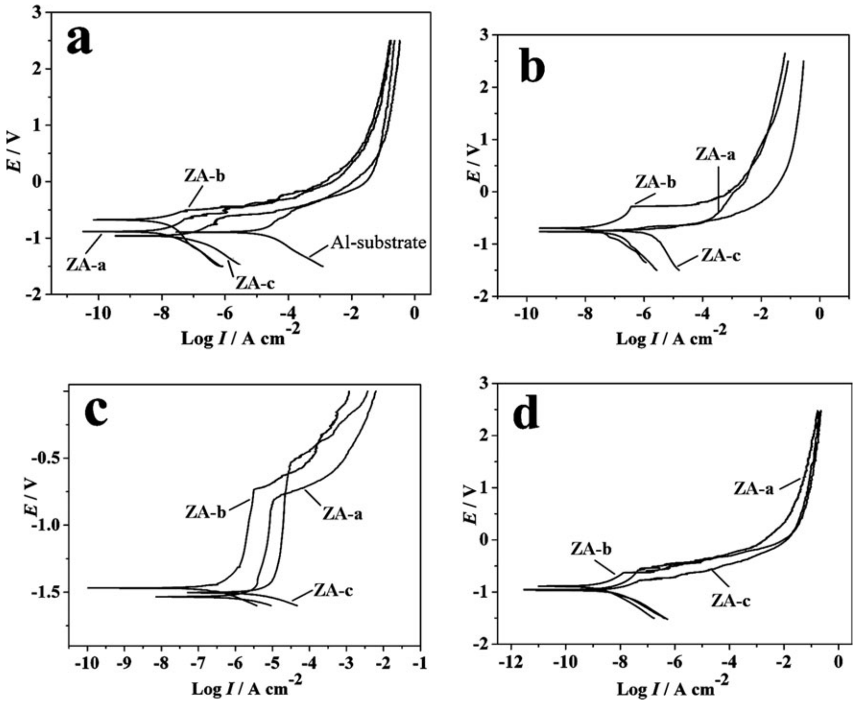

Figure 8. Polarization curves of samples immersed in neutral 3.5% aqueous sodium chloride solution (a), immersed in acidic solutions (b), immersed in basic solutions (c), and immersed in neutral 3.5% aqueous sodium chloride solution after surface hydrophobization (d).

to be less changed after being immersed in the corrosive medium for 30 days. The above results confirm the significant corrosion-resistant properties of as-fabricated $ZnAl_2O_4$ films due to the formation of passive layer. Compared with those in neutral 3.5% aqueous sodium chloride solution, the polarization currents of $ZnAl_2O_4$ films are basically unchanged in acidic solutions (pH = 2; Figure 8b), and less than 10^{-7} A cm^{-2} in basic solutions (pH = 12; Figure 8c). Furthermore, after surface hydrophobization treatment with sodium laurate, the polarization measurements of $ZnAl_2O_4$ films reveal that the hydrophobic $ZnAl_2O_4$ films give lower current densities below 10^{-9} A cm^{-2} (Figure 8d), compared to the hydrophilic $ZnAl_2O_4$ films. It suggests that the hydrophobic $ZnAl_2O_4$ films provide more effective corrosion-resistant coating, which originates from the superior barrier ability to corrosive ion migration.

EIS measurements are also used to better characterize the protective behavior of the $ZnAl_2O_4$ films. The Nyquist plots of ZA-a, ZA-b, ZA-c, and bare Al substrate subject to neutral 3.5% aqueous sodium chloride solution are shown in Figure 9a. It can be seen that the impedance spectrum of as-fabricated samples consist of two semicircles and a sloping line. The electrochemical impedance of $ZnAl_2O_4$ films is approximately two orders of magnitude larger than that of bare Al substrate. Especially, compared to ZA-a and ZA-c samples, ZA-b sample exhibits higher electrochemical impedance, indicating that ZA-b has larger charge resistance to ion migration. Figure 9b shows the typical Bode plot of ZA-b sample. The high-frequency time-dependent component at about 10^4 Hz is related to Faradic charge-transfer process of the surface $ZnAl_2O_4$ layer extending from the dense intermediate oxide barrier layer to the outermost surface of the film, and the time component at about 1 Hz originates from the capacitance of the intermediate oxide barrier layer adjoining the metal film. The low-frequency time-dependent component at 0.01 Hz (Warburg impedance) originates from the

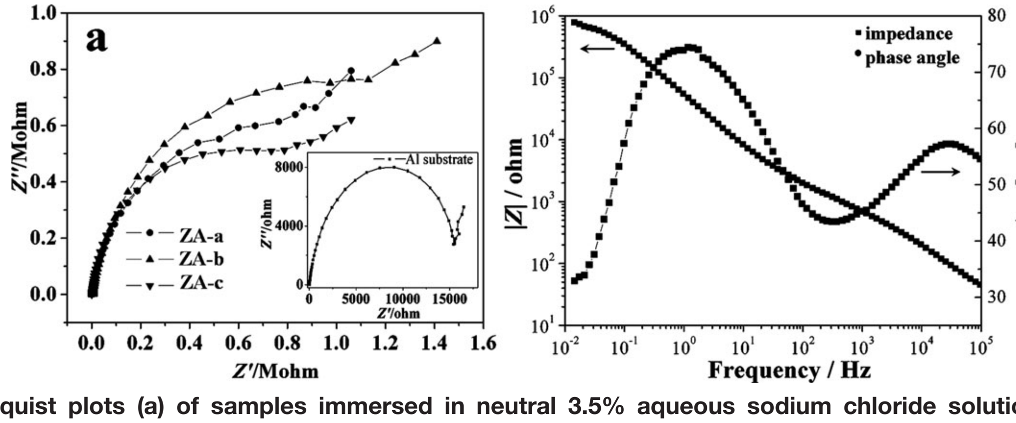

Figure 9. Nyquist plots (a) of samples immersed in neutral 3.5% aqueous sodium chloride solution, and typical Bode plot (b) of ZA-b sample.

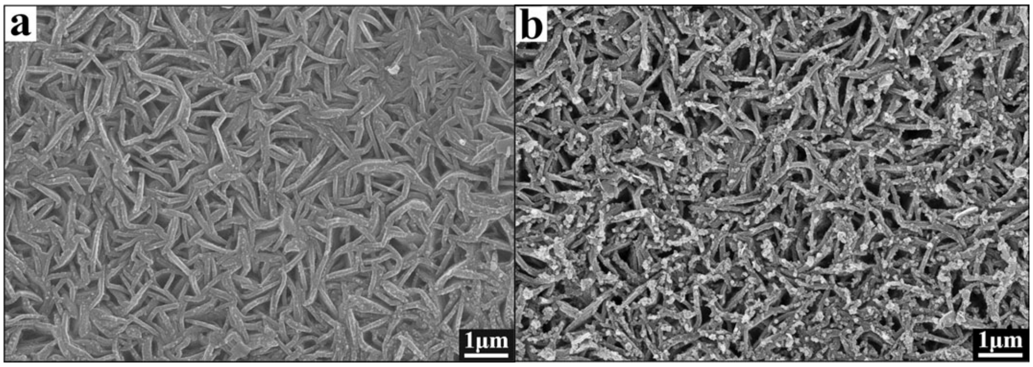

Figure 10. FESEM micrographs of ZA-b sample: before (a) and after (b) immersion in 3.5% aqueous sodium chloride solution for 30 days.

diffusion of corrosive reactants or species produced by corrosion through a passive layer with a high charge-transfer resistance.[61,62]

It is well-known that high adhesion of the anticorrosion coating to the metal substrate is essential for practical applications. FESEM micrographs of ZA-b sample show the unchanged surface microstructure after long-term immersion in 3.5% aqueous sodium chloride solution for 30 days (Figure 10). Meanwhile, after cross-cutting through the surface of ZA-b film, no significant peeling or delamination is observed (Figure 11). The above result confirms excellent chemical stability and strong adhesion of as-fabricated $ZnAl_2O_4$ film, which is attributed to direct growth of $ZnAl_2O_4$ crystallites from substrate.

In general, ZA-b sample shows the highest anticorrosion ability, and the order of corrosion-resistant ability obtained is ZA-b > ZA-a > ZA-c. It is well-known that the rate of corrosion and the diffusion of chloride ions are determined by the size of pore pathways. In the present system, a dense surface structure for compact nanorod-assembled $ZnAl_2O_4$ film with few pores can provide good resistance to the transportation of ions and electrons, thus, resulting in superior corrosion-resistant ability for the underlying aluminum substrate. A more accessible porous structure for ZA-a (nanoparticle assembled) and ZA-c (nanosword assembled), however, may allow the electrolyte to penetrate toward the metal surface and, thus, initiate the corrosion processes more easily.

Conclusions

$ZnAl_2O_4$ thin films with controlled surface microstructure have been successfully fabricated on aluminum substrates by a simple one-step *in situ* crystallization approach. The growth of $ZnAl_2O_4$ nanostructures including nanoparticles, nanorods, and nanoswords was found to be greatly affected by the concentration of Zn^{2+} and urea under the solvothermal conditions. Polarization measurements revealed that the nanorod-assembled $ZnAl_2O_4$ film with strong adhesion to the aluminum substrate could effectively protect the aluminum from corrosion in a wide range of pH values, and that very low corrosion current densities of the order of $\sim 10^{-9}$ A cm^{-2} could be achieved. EIS results showed that the $ZnAl_2O_4$ film could serve as a passive layer with a high charge-transfer resistance contributing to its anticorrosion ability. Based on these properties of the as-fabricated $ZnAl_2O_4$ film as well as nontoxic nature, it is expected that the $ZnAl_2O_4$ film has the potential to become an environmentally friendly alternative for increasingly regulated chromate coatings.

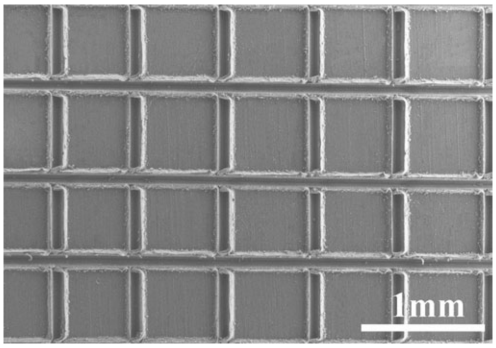

Figure 11. FESEM micrograph of ZA-b sample tested for adhesion.

Acknowledgments

This work was financially supported by the 973 Program (2011CBA00506) and National Natural Science Foundation of China.

Literature Cited

1. Cao MH, Dierdi I, Antonietti M, Niederberger M. Nonaqueous synthesis of colloidal $ZnGa_2O_4$ nanocrystals and their photoluminescence properties. *Chem Mater*. 2007;19:5830–5832.
2. Sampath SK, Cordaro JF. Optical properties of zinc aluminate, zinc gallate, and zinc aluminogallate spinels. *J Am Ceram Soc*. 1998;81:649–654.
3. Dutta DP, Ghildiyal R, Tyagi AK. Luminescent properties of doped zinc aluminate and zinc gallate white light emitting nanophosphors prepared via sonochemical method. *J Phys Chem C*. 2009;113:16954–16961.
4. Xue H, Li ZH, Ding ZX, Wu L, Wang XX, Fu XZ. Hollow rods of nanocrystalline $NiGa_2O_4$: hydrothermal synthesis, formation mechanism, and application in photocatalysis. *Cryst Growth Des*. 2008;8:4511–4516.
5. Fan GL, Gu ZJ, Yang L, Li F. Nanocrystalline zinc ferrite photocatalysts formed using the colloid mill and hydrothermal technique. *Chem Eng J*. 2009;115:534–541.
6. Xiong WZ, Kale GM. Electrochemical NO_2 sensor using a $NiFe_{1.9}Al_{0.1}O_4$ oxide spinel electrode. *Anal Chem*. 2007;79:3561–3567.
7. Kim CH, Myung Y, Cho YJ, Kim HS, Park S-H, Park J. Electronic structure of vertically aligned Mn-doped $CoFe_2O_4$ nanowires and their application as humidity sensors and photodetectors. *J Phys Chem C*. 2009;113:7085–7090.
8. Kim J, Kim HS, Lee N, Kim T, Kim H, Yu T, Song IC, Moon WK, Hyeon T. Multifunctional uniform nanoparticles composed of a magnetite nanocrystal core and a mesoporous silica shell for magnetic resonance and fluorescence imaging and for drug delivery. *Angew Chem Int Ed*. 2008;47:8438–8441.

9. Scarberry KE, Dickerson EB, MacDonald JF, Zhang ZJ. Magnetic nanoparticle-peptide conjugates for in vitro and in vivo targeting and extraction of cancer sells. *J Am Chem Soc*. 2008;130:10258–10262.
10. Wang M, Ai ZH, Zhang LZ. Generalized preparation of porous nanocrystalline $ZnFe_2O_4$ superstructures form zinc ferrioxalate precursor and its superparamagnetic property. *J Phys Chem C*. 2008; 112:13163–13170.
11. Wang ZL, Liu XJ, Lv MF, Chai P, Liu Y, Meng J. Preparation of ferrite MFe_2O_4 (M = Co, Ni) ribbons with nanoporous structure and their magnetic properties. *J Phys Chem B*. 2008;112: 11292–11297.
12. Bocanegra S, Ballarini A, Zgolicz P, Scelza O, De Miguel S. Highly selective and stable bimetallic catalysts supported on different materials for *n*-butane dehydrogenation. *Catal Today*. 2009;143:334–340.
13. Nilsson M, Jansson K, Jozsa P, Pettersson LJ. Catalytic properties of Pd supported on $ZnO/ZnAl_2O_4/Al_2O_3$ mixtures in dimethyl ether autothermal reforming. *Appl Catal B*. 2009;86:18–26.
14. Bocanegra SA, Guerrero-Ruiz A, Miguel SR, Scelza OA. Performance of PtSn catalysts supported on MAl_2O_4 (M: Mg or Zn) in *n*-butane dehydrogenation: characterization of the metallic phase. *Appl Catal A*. 2004;277:11–22.
15. Hu LH, Peng Q, Li YD. Selective synthesis of Co_3O_4 nanocrystal with different shape and crystal plane effect on catalytic property for methane combustion. *J Am Chem Soc*. 2008;130:16136–16137.
16. Grabowska H, Miśta W, Trawczyński J, Wrzyszcz J, Zawadzki M. A method for obtaining thymol by gas phase catalytic alkylation of *m*-cresol over zinc aluminate spinel. *Appl Catal A*. 2001;220:207–213.
17. Grabowska H, Zawadzki M, Syper L. Gas phase alkylation of 2-hydroxypyridine with methanol over hydrothermally synthesized zinc aluminate. *Appl Catal A*. 2006;314:226–232.
18. Bae SY, Lee J, Jung H, Park J, Ahn JP. Helical structure of single-crystalline $ZnGa_2O_4$ nanowires. *J Am Chem Soc*. 2005;127:10802–10803.
19. Fan HJ, Yang Y, Zacharias M. ZnO-based ternary compound nanotubes and nanowires. *J Mater Chem*. 2009;19:885–900.
20. Yang Y, Kim DS, Scholz R, Knez M, Lee SM, Gösele U, Zacharias M. Hierarchical three-dimensional ZnO and their shape-preserving transformation into hollow $ZnAl_2O_4$ nanostructures. *Chem Mater*. 2008;20:3487–3494.
21. Huang ZB, Zhu Y, Zhang JH, Yin GF. Stable biomimetic superhydrophobicity and magnetization film with Cu-ferrite nanorods. *J Phys Chem C*. 2007;111:6821–6825.
22. Zhang WW, Zhang JY, Chen ZY, Wang TM. Photocatalytic degradation of methylene blue by $ZnGa_2O_4$ thin films. *Catal Commun*. 2008;10:1781–1785.
23. Zou L, Li F, Xiang X, Evans DG, Duan X. Self-generated template pathway to high-surface-area zinc aluminate spinel with mesopore network from a single-source inorganic precursor. *Chem Mater*. 2006;18:5852–5859.
24. Zou L, Xiang X, Wei M, Li F, Evans DG. Single-crystalline $ZnGa_2O_4$ spinel phosphor via a single-source inorganic precursor route. *Inorg Chem*. 2008;47:1361–1369.
25. Khenata R, Sahnoun M, Baltache H, Rérat M, Reshak AH, Al-Douri Y, Bouhafs B. Full-potential calculations of structural, elastic and electronic properties of $MgAl_2O_4$ and $ZnAl_2O_4$ compounds. *Phys Lett A*. 2005;344:271–279.
26. Yang Y, Kim DS, Knez M, Scholz R, Berger A, Pippel E, Hesse D, Gösele U, Zacharias M. Influence of temperature on evolution of coaxial ZnO/Al_2O_3 one-dimensional heterostructures: from core-shell nanowires to spinel nanotubes and porous nanowires. *J Phys Chem C*. 2008;112:4068–4074.
27. Zhang D, Fu Z, Guo J. Microstructure and temperature distribution in $ZnAl_2O_4$ sintered body by pulse electric current. *J Mater Sci Technol*. 2003;19:526–528.
28. Van der Laag NJ, Snel MD, Magusin PCMM, de With G. Structural, elastic, thermophysical and dielectric properties of zinc aluminate ($ZnAl_2O_4$). *J Eur Ceram Soc*. 2004;24:2417–2424.
29. Wang Y, Wu K. As a whole: crystalline zinc aluminate nanotube array-nanonet. *J Am Chem Soc*. 2005;127:9686–9687.
30. Mathur S, Veith M, Haas M, Shen H, Lecerf N, Huch V, Hüfner S, Haberkorn R, Beck HP, Jilavi M. Single-source sol-gel synthesis of nanocrystalline $ZnAl_2O_4$: structural and optical properties. *J Am Ceram Soc*. 2001;84:1921–1928.
31. Wei XH, Chen DH. Synthesis and characterization of nanosized zinc aluminate spinel by sol-gel technique. *Mater Lett*. 2006;60:823–827.
32. Chen XY, Ma C, Zhang ZJ, Wang BN. Ultrafin gahnite ($ZnAl_2O_4$) nanocrystals: hydrothermal synthesis and photoluminescent properties. *Mater Sci Eng B*. 2008;151:224–230.
33. Zawadzki M, Wrzyszcz J. Hydrothermal synthesis of nanoporous zinc aluminate with high surface area. *Mater Res Bull*. 2000;35: 109–114.
34. Chen ZZ, Shi E, Li WJ, Zheng YQ, Wu NC, Zhong WZ. Particle size comparison of hydrothermally synthesized cobalt and zinc aluminate spinels. *J Am Ceram Soc*. 2002;85:2949–2955.
35. Phani AR, Passacantando M, Santucci S. Synthesis and characterization of zinc aluminum oxide thin films by sol-gel technique. *Mater Chem Phys*. 2001;68:66–71.
36. Wu YQ, Du J, Choy KL, Hench LL, Guo JK. Formation of interconnected microstructural $ZnAl_2O_4$ films prepared by sol-gel method. *Thin Solid Films*. 2005;472:150–156.
37. Lou ZD, Hao JH. Cathodoluminescence of rare-earth-doped zinc aluminate films. *Thin Solid Films*. 2004;450:334–340.
38. Tian XQ, Wan LJ, Pan K, Tian CG, Fu HG, Shi KY. Facile synthesis of mesoporous $ZnAl_2O_4$ thin films through the evaporation-induced self-assembly method. *J Alloys Compd*. 2009;488:320–324.
39. Szalarska-Smialowska Z. Pitting corrosion of aluminum. *Corros Sci*. 1999;41:1743–1767.
40. Liu Z, Chong PH, Butt AN, Skeldon P, Thompson GE. Corrosion mechanism of laser-melted AA2014 and AA2024 alloys. *Appl Surf Sci*. 2005;247:294–299.
41. Kuznetsova A, Burleigh TD, Zhukov V, Blachere J, Yates JT. Electrochemical evaluation of a new type of corrosion passivation layer: artificially produced Al_2O_3 films on aluminum. *Langmuir*. 1998;14:2502–2507.
42. Xin SG, Song LX, Zhao RG, Hu XF. Influence of cathodic current on composition, structure and properties of Al_2O_3 coatings on aluminum alloy prepared by micro-arc oxidation process. *Thin Solid Films*. 2006;515:326–332.
43. Sauvant-Moynot V, Gonzalez S, KIttel J. Self-healing coatings: an alternative route for anticorrosion protection. *Prog Org Coat*. 2008;63:307–315.
44. Lamaka SV, Shchukin DG, Andreeva DV, Zheludkevich ML, Möhwald H, Ferreira MGS. Sol-gel/polyelectrolyte active corrosion protection system. *Adv Funct Mater*. 2008;18:3137–3147.
45. Chidambaram D, Clayton CR, Halada GP. Interactions of the components of chromate conversion coating with the constituents of aluminum alloy AA2024-T3. *J Electrochem Soc*. 2004;151:151–159.
46. Chidambaram D, Clayton CR, Halada GP. The role of hexafluorozirconate in the formation of chromate conversion coatings on aluminum alloys. *Electrochim Acta*. 2006;51:2862–2871.
47. Chen ZZ, Shi EW, Zheng YQ, Li WJ, Xiao B, Zhuang JY, Tang LA. Particle size control and dependence on precursor pH: synthesis uniform submicrometer zinc aluminate particles. *J Am Ceram Soc*. 2005;88:127–133.
48. Fu Q, Rao GVR, Basame SB, Keller DJ, Artyushkova K, Fulghum JE, Lopez GP. Reversible control of free energy and topography of nanostructured surfaces. *J Am Chem Soc*. 2004;126: 8904–8905.
49. Xie Q, Xu J, Feng L, Jiang L, Tang W, Luo X, Han CC. Facile creation of a super-amphiphobic coating surface with bionic microstructure. *Adv Mater*. 2004;16:302–305.
50. Li HJ, Wang XB, Song YL, Liu YQ, Li QS, Jiang L, Zhu DB. Super-"amphiphobic" aligned carbon nanotube films. *Angew Chem Int Ed*. 2001;40:1743–1746.
51. Chang CL, Sankaranarayanan SKRS, Engelhard M, Shutthanandan V, Ramanathan S. On the relationship between nonstoichiometry and passivity breakdown in ultrathin oxides: combined depth-dependent spectroscopy, Mott-Schottky analysis, and molecular dynamics simulation studies. *J Phys Chem C*. 2009;113: 3502–3511.
52. Kraus GF, Greer SC. Vapor pressures of supercooled H_2O and D_2O. *J Phys Chem*. 1984;88:4781–4785.
53. Banerjee S. Solubility of organic mixtures in water. *Environ Sci Technol*. 1984;18:587–591.
54. Vaseem M, Umar A, Kim SH, Hahn YB. Low-temperature synthesis of flower-shaped CuO nanostructures by solution process: formation mechanism and structural properties. *J Phys Chem C*. 2008;112:5729–5735.
55. Zhang J, Sun LD, Yin JL, Su HL, Liao CS, Yan CH. Control of ZnO morphology via a simple solution route. *Chem Mater*. 2002;14:4172–4177.
56. Koh YW, Lin M, Tan CK, Foo YL, Loh KP. Self-assembly and selected area growth of zinc oxide nanorods on any surface

promoted by an aluminum precoat. *J Phys Chem B*. 2004;108:11419–11425.
57. Liu B, Zeng HC. Semiconductor rings fabricated by self-assembly of nanocrystals. *J Am Chem Soc*. 2005;127:18262–18268.
58. Penn RL. Kinetics of oriented aggregation. *J Phys Chem B*. 2004;108:12707–12712.
59. Peng ZA, Peng XG. Mechanisms of the shape evolution of CdSe nanocrystals. *J Am Chem Soc*. 2001;123:1389–1395.
60. Veselý D, Kalendova A. Anticorrosion efficiency of $Zn_xMg_yAl_2O_4$ core-shell spinels in organic coatings. *Prog Org Coat*. 2008;62:5–20.
61. Roto R, Villemure G. Electrochemical impedance spectroscopy of electrodes modified with thin films of Ni–Al–Cl layered double hydroxides. *J Electroanal Chem*. 2002;527:123–130.
62. Zhang HP, Baldelli S. Alkanethiol monolayers at reduced and oxidized zinc surfaces with corrosion protection: a sum frequency generation and electrochemistry investigation. *J Phys Chem B*. 2006;110:24062–24069.

Manuscript received Apr. 8, 2011, and revision received Sept. 21, 2011.